Front. Chem. Sci. Eng. 2024, 18(11): 134
https://doi.org/10.1007/s11705-024-2485-2

RESEARCH ARTICLE

Enhanced formic acid production for CO_2 photocatalytic reduction over Pd/H-TiO_2 catalyst

Huimin Gao[1*], **Jinpeng Zhang**[1*], **Fangyuan Zhang**[1], **Jieying Jing** (✉)[1,2], **Wen-Ying Li** (✉)[1]

1 State Key Laboratory of Clean and Efficient Coal Utilization, Taiyuan University of Technology, Taiyuan 030024, China
2 Shanxi-Zheda Institute of Advanced Materials and Chemical Engineering, Taiyuan 030000, China

Abstract The photocatalytic reduction of CO_2 into formic acid is a feasible approach to alleviate the effects of global climate change and achieve chemical energy storage. It is important to design highly active photocatalysts to improve the selectivity and yield of formic acid. In this study, TiO_2-based catalysts were prepared and loaded with Pd nanoparticles via an impregnation process. The Pd/H-TiO_2 catalyst demonstrated superior CO_2 reduction activity and a high formic acid production rate of 14.14 $mmol_{cat}\cdot g^{-1}\cdot h^{-1}$. The excellent catalytic performance observed in the presence of a Pd/H-TiO_2 catalyst is ascribed to the synergy between O_v and Pd. The presence of O_v led to increase in CO_2 adsorption while Pd loading enhanced the photogenerated electron-hole pair separation. Electron transfer from H-TiO_2 to Pd also contributed to CO_2 activation.

Keywords CO_2 reduction, formic acid, photocatalysis, TiO_2 catalyst

1 Introduction

CO_2 emissions from fossil fuel combustions result in numerous severe environmental problems [1]. The conversion of CO_2 into carbon-containing solar fuels is a promising technology to alleviate the harmful effects of global climate change. CO_2 can be converted into various chemicals, including CO, CH_3OH, HCOOH, and CH_4 [2]. Among them, HCOOH is widely studied owing to its considerable market demand and high energy density [3]. For example, it possesses a remarkable volumetric hydrogen storage density of 53 $g\cdot L^{-1}$, which is equivalent to 600 times of compression hydrogen; as such, HCOOH can be used as a hydrogen storage molecule [4]. Several pathways exist for the conversion of CO_2 into chemicals [5], including photocatalytic reduction, thermochemical reduction, biochemical reduction, and electrochemical reduction. The photocatalytic reduction of CO_2 does not require further thermal energy input; it conducts a conversion reaction through the transfer of electrons generated by the catalyst being excited by light to CO_2. However, the photocatalytic reduction of CO_2 is a multiple-electron transfer process involving complex reaction pathways and yields different products depending on the number of electrons transferred [6], resulting in poor product selectivity and a low efficiency in producing HCOOH. Therefore, to achieve highly selective HCOOH synthesis and increase the production rate of HCOOH, it is imperative to design photocatalysts with conduction potentials close to the redox potential of HCOOH.

Many inorganic semiconductor materials, such as doped Al_2O_3 [7], ZnO, and TiO_2 have been applied to CO_2 photocatalytic reduction for producing HCOOH [8]. Among them, TiO_2 is one of the most popular materials and exhibits excellent photocatalytic performance owing to its suitable redox potential. However, TiO_2 exhibits a low photocatalytic reduction efficiency owing to its large band gap and rapid electron-hole recombination [9]. Furthermore, TiO_2 has a high redox potential, resulting in the occurrence of side reactions and difficulties in obtaining HCOOH with high selectivity. To overcome these limitations, several strategies have been studied, including metal loading, semiconductor coupling, dye sensitization, and construction defect engineering [10]. Among them, metal loading and vacancy defect construction in semiconductors are two effective approaches to slow down electron-hole recombination [11].

Research has shown that the formation of oxygen vacancies (O_v) considerably affects photocatalytic CO_2 reduction performance [12,13]. The formation of O_v increases CO_2 adsorption and thereby enhances

---

Received April 4, 2024; accepted May 15, 2024; online August 5, 2024

E-mails: jingjieying@tyut.edu.cn (Jing J), ying@tyut.edu.cn (Li W-Y)

*These authors contributed equally to this work.

photocatalytic CO_2 reduction efficiency. Zhao et al. [14] summarized how defective sites improve the photocatalytic reduction of CO_2 and confirmed that formation of O_v on the TiO_2 surface can enhance the adsorption and conversion of CO_2. However, merely promoting CO_2 adsorption is insufficient to enhance the photocatalytic CO_2 reduction efficiency. Efficient photoelectron transfer is another key factor in improving photocatalytic CO_2 reduction performance. The rapid photogenerated electron-hole recombination in TiO_2 causes low photocatalytic CO_2 reduction activity [15]. Modifying TiO_2 with metal is not only an effective and direct method to reduce the band gap of TiO_2 but can also slow down the recombination of photogenerated electron-hole pairs, thereby resulting in improved photocatalytic activity. Recently, metal cocatalysts, such as Pt [16], Pd [17], and Ag [18] have been employed in photocatalytic CO_2 reduction. The Schottky junction formed by loading metals on semiconductors can trap photogenerated electrons, after which the separated electrons are transferred to the surface of the catalyst for CO_2 conversion, thereby considerably increasing the photocatalytic efficiency [19]. Li et al. [11] designed a Ag/TiO_2 catalyst via a hydrothermal process involving *in situ* photodeposition; their results demonstrated increased photocatalytic CO_2 reduction activity, which was attributed to the combined effect of Ag and defective TiO_2.

Herein, we prepared TiO_2-based catalysts and investigated how O_v and Pd influenced CO_2 adsorption and activation and thereby improved the photocatalytic activity. Hydrogen pretreatment was found to lead to the incorporation of H atoms into O_v, forming Ti–H bonds to guarantee the high selectivity of HCOOH. Characterizations and density functional theory (DFT) calculations confirmed that O_v increases the CO_2 adsorption capacity of TiO_2 and that loaded Pd particles can trap photogenerated electrons from semiconductors to promote electron-hole separation.

2 Experimental

2.1 Materials

Anatase TiO_2 (99.8%), $PdCl_2$ (99.9%), $NaBH_4$ (98%), K_2CO_3 (98%), KOH (95%), $KHCO_3$ (99.5%), and a standard HCOOH solution (analytic grade) were purchased from Shanghai Aladdin Reagent Co., China.

2.2 Catalyst synthesis

Anatase TiO_2 was employed as a precursor without any treatment (hereafter referred to as TiO_2). Hydrogenated TiO_2 (H-TiO_2) was obtained by pretreating TiO_2 in a 5 vol % H_2/Ar atmosphere at 500 °C for 12 h. Based on the pretreatment temperature, the obtained catalysts were denoted as H-TiO_2-T (where T represents hydrogenation temperature).

The Pd/H-TiO_2 catalyst was fabricated via impregnation [20]. In particular, $PdCl_2$ (0.0284 mmol), H-TiO_2 (0.5 g), and deionized water (20 mL) were mixed in a beaker. The obtained substance was stirred for 24 h at 25 °C until a well-dispersed suspension was obtained; subsequently, a 1 $mol \cdot L^{-1}$ aqueous NaOH solution was used to adjust the pH of the suspension to 10.0–11.0. A 30 $mg \cdot mL^{-1}$ aqueous $NaBH_4$ solution was added to the obtained alkaline suspension at a molar ratio of $n(Pd):n(NaBH_4) = 1:6$, followed by stirring for 2 h until no bubble production occurred. A solid substance was separated from the resultant suspension via filtration and washed with water to remove any residual material; subsequently, the washed solid substance was baked at 110 °C for 12 h to produce a sample, which was termed Pd/H-TiO_2.

2.3 Catalyst characterization

The crystalline structures of the TiO_2, H-TiO_2, and Pd/H-TiO_2 catalysts were analyzed via X-ray diffraction (XRD, Rigaku Ultima IV). The Pd content of the Pd/H-TiO_2 catalyst was monitored via inductively coupled plasma-optical emission spectrometry (ICP-OES; Agilent 5110). Transmission electron microscopy (TEM) and high-resolution TEM (HRTEM) were performed using a JEOL JEM 2100F transmission electron microscope to determine the morphology and metal particle size of the synthesized catalysts. The electronic valence states of the elements in the prepared catalysts were evaluated via X-ray photoelectron spectroscopy (XPS, Thermo Scientific K-Alpha). The photoelectric chemical properties of the prepared catalysts were analyzed using an electrochemical workstation (CHI 760E). Photoluminescence spectra (PL spectra) were obtained to analyze the separation efficiency of the photogenerated electron-hole pairs. FLUKE infrared imaging was used to detect the temperature distribution of the sample surface in a noncontact manner throughout this process, and images were obtained. O_v characterization of the catalyst surface was performed via electron paramagnetic resonance spectrometry (EPR, Bruker EMX PLUS). The CO_2 adsorption capacity of the catalyst was recorded via CO_2 temperature-programmed desorption (CO_2-TPD, Micromeritics AutoChem II 2920).

2.4 CO_2 hydrogenation performance

The photocatalytic reduction of CO_2 was performed at 30 °C and 2.0 MPa in an autoclave reactor (50 mL, Anhui Kemi Machinery Technology Co., Ltd.) equipped with a sapphire window. Deionized water (10 mL), KOH (10 mL), and catalyst (2 $g \cdot L^{-1}$) were mixed in the autoclave reactor, which was then sealed. The residual air was displaced with CO_2 three times. Subsequently, 1.0 MPa CO_2 and 1.0 MPa H_2 were fed into the sealed reactor and 300 nm ultraviolet (UV) light was used as the light source for vertical exposure through the window inside the reactor. Temperature was precisely controlled using the thermocouple of the tank reactor. The experimental diagram is shown in Fig. S1 (cf. Electronic Supplementary Material, ESM). The resulting liquid products were detected using high-performance liquid chromatography (Agilent 1260). The rate of HCOOH production was calculated using Eq. (1) as follows:

$$Y = \frac{n_{\mathrm{HCOOH}}}{m_{\mathrm{cat.}} \times t}, \quad (1)$$

where n_{HCOOH} represents the amount of HCOOH after the reaction (mmol), $m_{\mathrm{cat.}}$ represents the catalyst mass (g), and t represents the reaction time (h).

2.5 Theoretical calculations

Simulation calculations based on DFT were used to investigate the effect of O_v and metal Pd loading on CO_2 adsorption and activation. The TiO_2 (101) surface was modeled based on HRTEM characterization. All calculations were performed using the Vienna Ab initio Simulation Package, applying the projector augmented wave (PAW) method [21,22]. Interactions between core and valence electrons was analyzed by PAW. To determine the total energy, a cutoff energy of 400 eV was set for plane wave basis sets, through which the valence electronic states were expanded. The convergence criterion for the self-consistent electronic loop was set at 10^{-5} eV. When the maximum force received by the atom was less than 0.02 eV·Å^{-1}, the calculation was considered to have converged. The Monkhorst-Pack k network was specified as 2 × 2 × 1 on the TiO_2 (101) surface with a vacuum thickness of 15 Å. The adsorption energy (E_{ads}) of CO_2 on the catalyst was calculated using Eq. (2):

$$E_{\mathrm{ads}} = E_{\mathrm{total}} - E_{\mathrm{catalyst}} - E_{\mathrm{CO_2}}, \quad (2)$$

where E_{total} is the total energy of CO_2 adsorbed to Pd metal particles on the support, E_{catalyst} is the total energy of the Pd/H-TiO_2 system, and $E_{\mathrm{CO_2}}$ is the total energy of the gas molecules. The charge density difference ($\Delta\rho$) was calculated using Eq. (3):

$$\Delta\rho_{\mathrm{AB}} = \rho_{\mathrm{A}} - \rho_{\mathrm{B}}, \quad (3)$$

where $\Delta\rho_{\mathrm{AB}}$, ρ_{A}, and ρ_{B} denote charge densities of the systems AB (CO_2 adsorbed on Pd/H-TiO_2), A (CO_2 or CO_2-Pd of CO_2 adsorbed on Pd/H-TiO_2), and B (Pd/H-TiO_2 or H-TiO_2 of CO_2 adsorbed on Pd/H-TiO_2), respectively. It is important to note that since the roles played by Pd and TiO_2 in the system are not yet clear, their interactions and the charge transfers between them were considered separately.

3 Results and discussion

3.1 Catalyst properties

Figure 1(a) shows XRD information of TiO_2, H-TiO_2, and Pd/H-TiO_2 catalysts. Changes in the crystalline structure of TiO_2 resulted from pretreatment at different temperatures. When compared with TiO_2, the diffraction peak crystallinity corresponding to the (101) plane decreased as the hydrogenation temperature increased from 400 to 600 °C. The characteristic peak at 27.58° matched with that of rutile TiO_2, indicating that the crystalline structure of H-TiO_2 gradually transformed from anatase to rutile with increasing temperature [23]. Previous investigations revealed that the rutile phase could inhibit the photocatalytic activity [24]. Therefore, Pd/H-TiO_2 was prepared via hydrogen pretreatment at 500 °C. The Pd/H-TiO_2 catalyst exhibited three major characteristic peaks at 25.3°, 37.9°, and 48.1°, which correspond to the (101), (004), and (200) planes, respectively (JCPDS No. 21-1272). The diffraction peaks of Pd were not observed, implying that Pd was highly dispersed on H-TiO_2 [25]. Furthermore, it was clear that the Pd/H-TiO_2 catalyst had characteristic diffraction peaks similar to those of H-TiO_2, indicating that Pd loading did not alter the crystal structure of anatase TiO_2 [26]. The main characteristic peaks, i.e., (101), (004), and (200), exhibited minimal shift, indicating that Pd did not enter the lattice of H-TiO_2; instead, it was highly dispersed on the surface [20]. The micromorphology and crystalline phase of the TiO_2, H-TiO_2, and Pd/H-TiO_2 catalysts were verified using TEM. As shown in Fig. 1(b), the O_v from hydrogen treatment and Pd loading did not affect the morphology, and Pd with an average diameter of 5 nm remained on H-TiO_2 and the TiO_2 catalysts. In addition, the Pd/H-TiO_2 catalyst exhibited a 0.22 nm lattice fringe spacing, as shown in HRTEM images (Fig. 1(c)), corresponding to Pd (111), and the lattice stripe spacing of anatase (101) was calculated to be 0.34 nm. As shown in Fig. 1(d), energy dispersive spectroscopy (EDS) analysis of the Pd/H-TiO_2 catalyst revealed that it contained Ti, O, and Pd, which were evenly distributed across the surface of H-TiO_2. According to the ICP-OES data shown in Table S1 (cf. ESM), the actual amount of Pd in the catalyst was consistent with the theoretical content obtained from the calculations, demonstrating that Pd nanoparticles were successfully loaded on H-TiO_2 using the impregnation method.

To further study the chemical compositions of various elements, including Pd, Ti, and O in the catalysts, the catalysts were examined using XPS. The resulting survey spectrum is shown in Fig. 2(a). Two characteristic peaks were observed at binding energies of 458.7 and 464.0 eV, which were assigned to Ti $2p_{3/2}$ and Ti $2p_{1/2}$ in TiO_2,

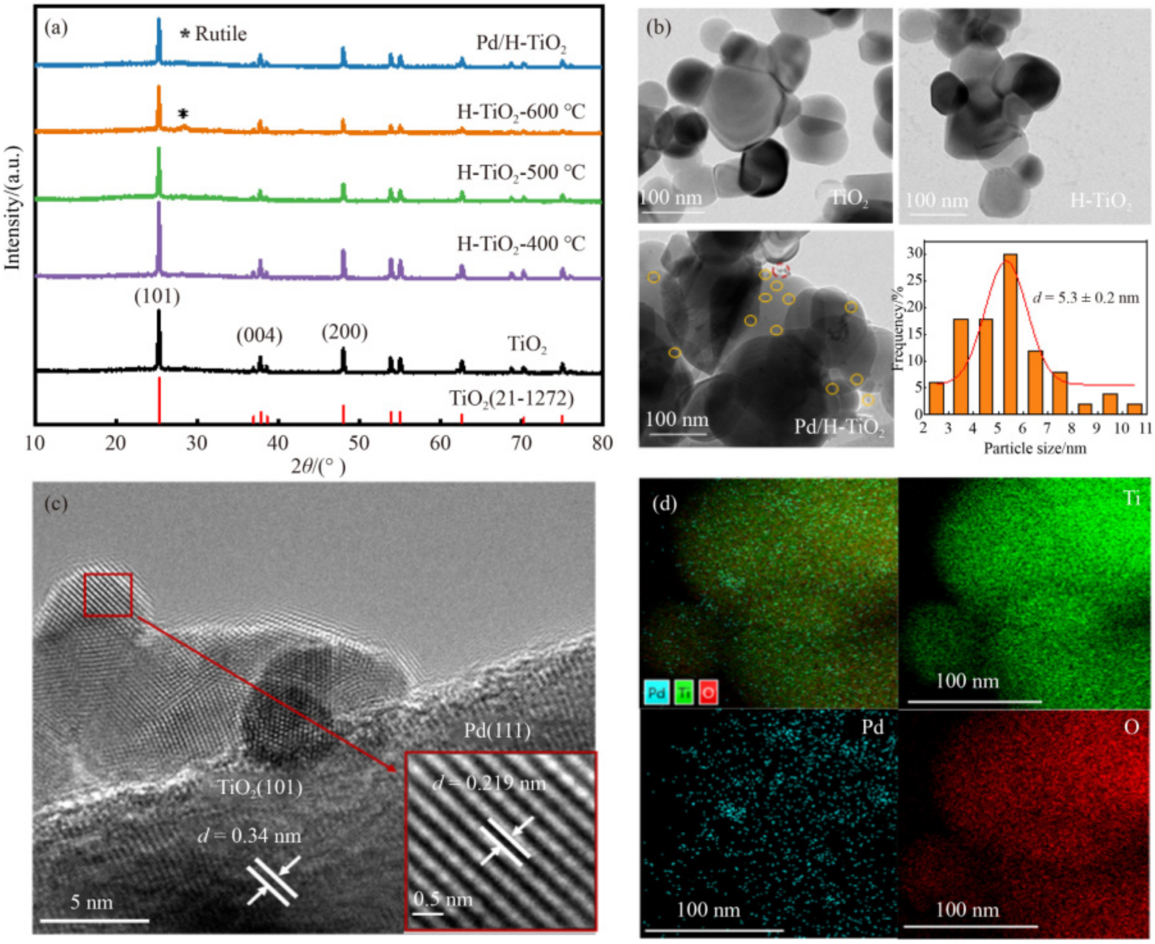

Fig. 1 (a) XRD patterns of TiO_2 at different hydrogenation temperatures and Pd/H-TiO_2, (b) TEM image of catalysts, (c) HRTEM image of Pd/H-TiO_2, (d) EDS elemental mapping of Pd/H-TiO_2.

respectively. In the XPS spectra of O 1s (Fig. 2(b)), the peak centered at ~531.7 eV was attributed to O_v. Because the lack of oxygen atoms in the sample can cause a change of chemical state, the metal ions must lower their valence state to remain electrically neutral. Accordingly, upon hydrogen treatment of TiO_2, in addition to Ti^{4+}, Ti^{3+} is formed in H-TiO_2 [27]. This indicates that hydrogen treatment of TiO_2 can produce partial O_v. Furthermore, the binding energy of Ti $2p_{3/2}$ in H-TiO_2 (458.5 eV) shifts toward lower binding energy relative to that of TiO_2 (458.7 eV), implying the formation of Ti–H bonds in H-TiO_2, which is in accordance with the phenomenon reported by Samsudin et al. [28]. We further conclude that the formation of Ti–H bonds occurs owing to the occupation of O_v by H atoms according to the results reported by Liu et al. [29]. The presence of H atoms can increase the electron density of the adjacent Ti, causing the binding energy to shift to lower energy regions [29,30]. As shown in Fig. 2(c), the peaks located at 334.6 and 339.9 eV match well with those of Pd $3d_{5/2}$ and Pd $3d_{3/2}$, respectively. Additionally, the spectral peaks of Pd were found to have shifted toward lower binding energies relative to the standard binding energy of Pd^0 (335.4 and 340.7 eV). Moreover, the binding energy of Ti shifted toward higher energies after Pd loading, signifying an interaction between Pd and H-TiO_2 and the transfer of electrons from H-TiO_2 to Pd [31].

EPR experiments were conducted to detect O_v in various photocatalysts, as shown in Fig. 2(d). The characteristic signal at a g value of 1.973 in TiO_2 denotes the presence of a metal species [32]. Following hydrogen treatment, a distinct characteristic signal was found at the g value of 2.002 for H-TiO_2 and Pd/H-TiO_2, corresponding to O_v on the surface of the material [33]. This result is consistent with the information obtained from XPS analysis.

3.2 Photocatalytic reduction of CO_2

3.2.1 Performance of photocatalytic reduction of CO_2 to HCOOH

The photocatalytic activities of the catalysts were evaluated at 30 °C, 2.0 MPa, and a light intensity of 4.57 $mW \cdot cm^{-2}$. It was found that the HCOOH production rate over untreated TiO_2 was only 0.83 $mmol \cdot g_{cat}^{-1} \cdot h^{-1}$ in Fig. 3(a). Following treatment with H_2, the HCOOH production rate on the H-TiO_2 catalyst reached

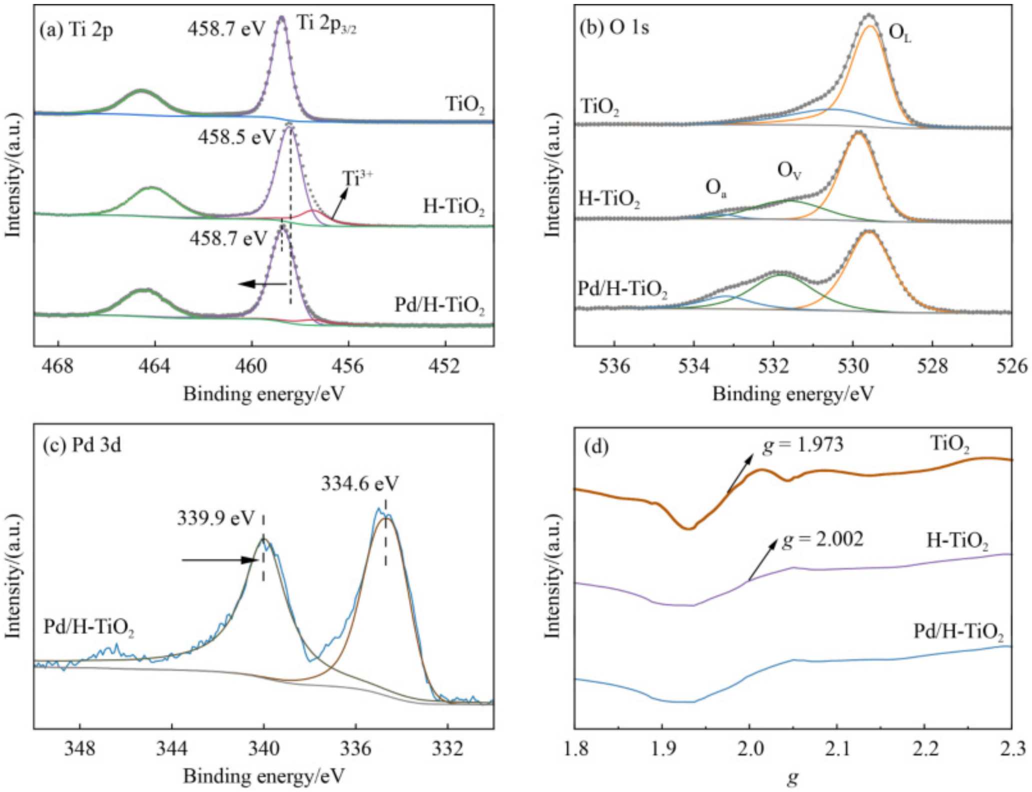

Fig. 2 XPS spectra of (a) Ti 2p, (b) O 1s, (c) Pd 3d, and (d) EPR of TiO_2, H-TiO_2, and Pd/H-TiO_2 obtained at room temperature.

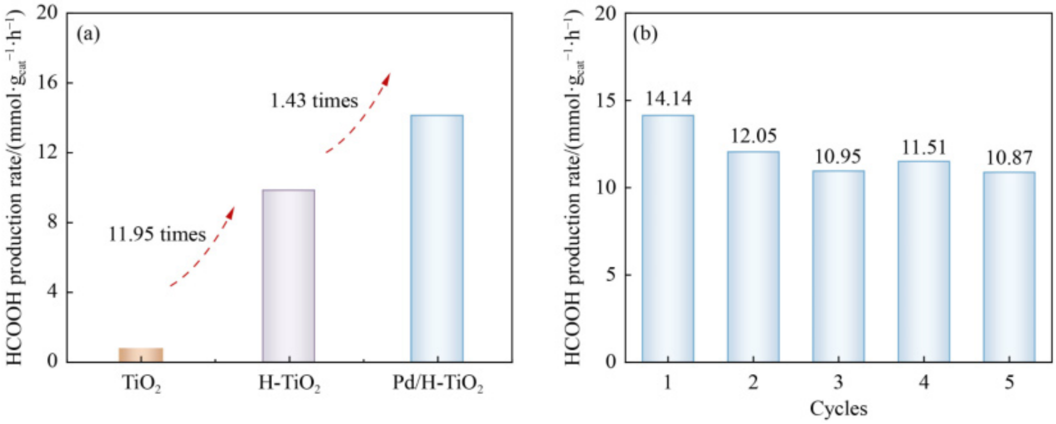

Fig. 3 (a) HCOOH production rate within 1 h with different catalysts, (b) cyclic stability of the Pd/H-TiO_2 catalyst.

9.86 mmol·g_{cat}^{-1}·h^{-1}, i.e., 11.95 times higher than that of TiO_2. Additionally, the reduction activity and HCOOH production rate (14.14 mmol·g_{cat}^{-1}·h^{-1}) of Pd/H-TiO_2 was superior to that of the other catalysts. Compared with TiO_2 and H-TiO_2, the total HCOOH production of Pd/H-TiO_2 also increased significantly within 3 h (Fig. S2, cf. ESM). Throughout the process, the gases before and after the reaction were collected and tested, showing that almost no other carbon-containing products were produced. As such, the selectivity of HCOOH was close to 100%. When the reaction was catalyzed by Pd/H-TiO_2, the HCOOH production rate showed a significant increase, comparable to recent reports (Table S2, cf. ESM) [34,35].

We further analyzed the reasons for the high selectivity and activity of HCOOH when using the Pd/H-TiO_2 catalyst. From XPS results (i.e., the binding energy of Ti in the TiO_2 catalyst was 458.7 eV), the binding energy of Ti $2p_{3/2}$ was found to shift toward lower values (458.5 eV) after hydrogen pretreatment, suggesting that most O_v was replaced by hydrogen and the Ti–H bond formed for higher HCOOH selectivity. This phenomenon had previously been demonstrated in a semiconductor catalysts system [29,36]. Furthermore, the CO_2 adsorption capacity of the catalyst was analyzed using CO_2-TPD as shown in Table S1. Compared to the TiO_2 catalyst, the adsorption of CO_2 over H-TiO_2 and Pd/H-TiO_2 reached 0.13 and 0.18 mmol·g^{-1}, respectively, demonstrating that

O_v could increase the CO_2 adsorption and further enhance the HCOOH yield.

Cycling experiments were conducted under the same conditions to evaluate the long-term stability of the Pd/H-TiO_2 catalyst. The results of the experiments indicated that the photocatalytic reduction of CO_2 activity decreased slightly after five cycles under UV light irradiation (Fig. 3(b)). To reveal the reason for the decrease of HCOOH yield, TEM analysis (Fig. S3, cf. ESM) was performed for the catalyst after running five cycles. Agglomeration of metal Pd particles was observed; this might cause the reformation of electron-hole recombination sites, leading to a decrease in the effective electrons number involved in the CO_2 conversion reaction. Consequently, a slight decrease in HCOOH production rate was observed after five cyclic reactions.

The optical absorption properties of the Pd/H-TiO_2 photocatalyst were determined using UV-vis diffuse-reflectance spectroscopy as shown in Fig. 4(a). According to the resulting Tauc plots, the band gap (E_g) for Pd/H-TiO_2 was estimated to be 2.7 eV (Fig. 4(b)). Mott-Schottky measurements were determined to investigate the band structure of the Pd/H-TiO_2 catalyst (Figs. 4(c) and 4(d)). The positive slope of the M-S curve confirmed that the prepared Pd/H-TiO_2 catalyst was an *n*-type semiconductor. The conduction band (CB) values of *n*-type semiconductors can be estimated using flat band values. Based on the data in Fig. 4(c), the flat band value of the Pd/H-TiO_2 catalyst with respect to the Ag/AgCl electrode was –0.96 V. The valence band (VB) values of the Pd/H-TiO_2 catalyst with respect to the normal hydrogen electrode (NHE) were obtained using formulas (4) and (5) [37] as follows:

$$E[vs.\ \mathrm{NHE}] = 0.2\ \mathrm{V} + E[vs.\ \mathrm{Ag/AgCl}], \tag{4}$$

$$E_{\mathrm{VB}} = E_{\mathrm{g}} + E_{\mathrm{CB}}. \tag{5}$$

It has been reported that the flat potential of *n*-type semiconductors was more positive by 0.1 V relative to the CB [38]. The flat band for the Pd/H-TiO_2 catalyst was −0.76 V *vs.* NHE. Thus, the calculated E_{CB} was −0.86 V *vs.* NHE and the E_{VB} of the Pd/H-TiO_2 catalyst was 1.84 V. This result demonstrates that Pd/H-TiO_2 catalyst meets the redox potential requirements for the photocatalytic reduction of CO_2 to HCOOH.

3.2.2 Microscopic interactions

To analyze the influence of O_v and Pd on CO_2 adsorption, the adsorption energy and differential charge density of CO_2 on TiO_2, H-TiO_2, and Pd/H-TiO_2 surfaces were studied using DFT calculations. Based on various experimental characterization methods, TiO_2, H-TiO_2, and Pd/H-TiO_2 models were constructed in Fig. S4 (cf. ESM) to reveal the mechanisms of interaction in CO_2 reduction systems. Due to differences in the coordination environments of Ti, oxygen vacancy sites were considered in terms of O_{v1} and O_{v2}. The structural information and

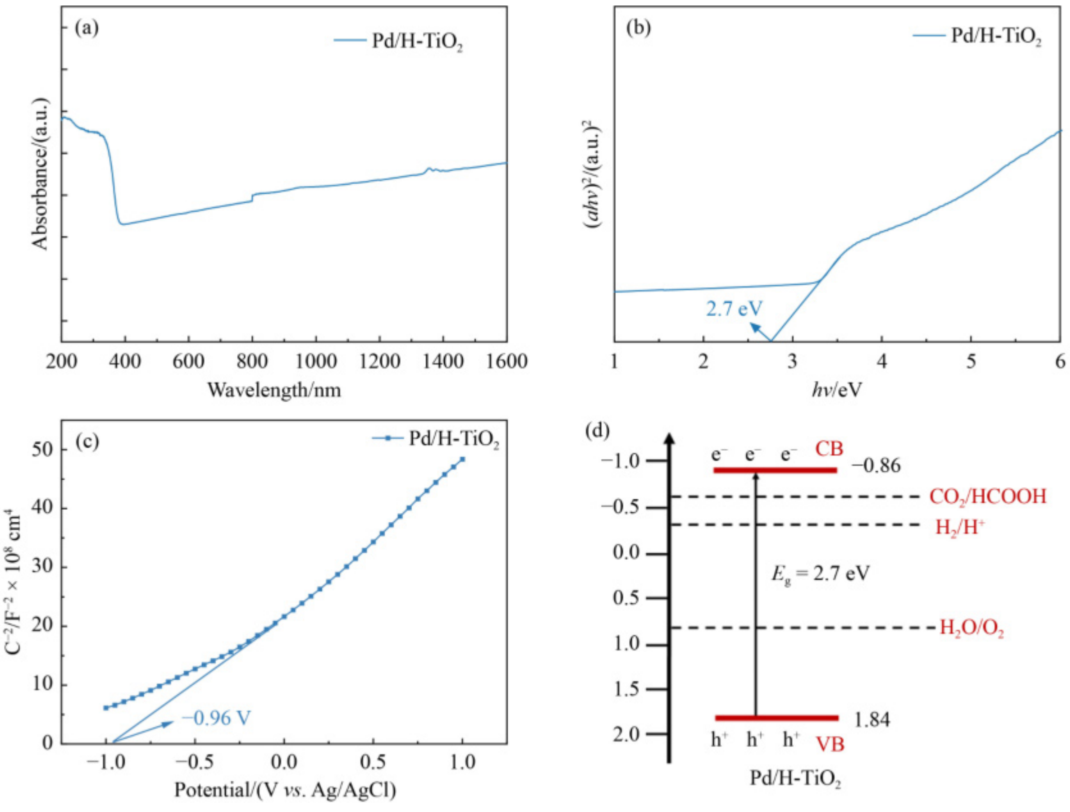

Fig. 4 (a) UV-vis spectra of various photocatalysts, (b) Tauc plots, (c) Mott-Schottky curves at 2000 Hz, (d) band structures.

adsorption energies of the models considered are listed in Table 1. The E_{ads} of CO_2 on the TiO_2 surface without O_v was approximately –0.104 eV, while the E_{ads} became more negative with the appearance of O_v on TiO_2, indicating that O_v boosted the interaction between CO_2 and the catalyst. In particular, a series of models with O_{v1} were found to have relatively stable CO_2 adsorption conformations, which was attributed to differences in O_v formation energy resulting from their different coordination environments. Although the E_{ads} of both O_{v1} and O_{v2} were negative, the experimental process was not easily achieved. Furthermore, the E_{ads} of H-TiO_2 with Pd was more negative than TiO_2 and H-TiO_2, with the exception of both O_{v1} and O_{v2} in a model. This phenomenon was attributed to the significant deformation of the Pd cluster structure caused by two O_v forms (Fig. S5(a), cf. ESM), which exhibited a higher adsorption energy value. These results demonstrated both that O_v significantly enhanced CO_2 adsorption and that Pd loading promoted adsorption and activation, agreeing with the characterization results of CO_2-TPD (Table S1).

The charge transfer during CO_2 adsorption activation process was further analyzed using charge differential density and Bader charge, as shown in Figs. 4(a–c). It is important to note that the direction of electron transfers between Pd, TiO_2, and CO_2 was not clear. Therefore, a detailed analysis of charge transfer between adjacent species was conducted by considering differential charge density. First, the charge transfers between CO_2 and the catalyst were considered, as shown in Figs. S6(a–d) (cf. ESM), showing that CO_2 gains electrons (approximately 0.4 e), consistent with previous reports indicating that it was more difficult to lose electrons from CO_2 while electron accumulation was more easily activated. Second, CO_2 and Pd were considered in the investigation of the charge transfer between Pd and TiO_2 (Figs. S7(a–d). The electron cloud intensity between Pd and TiO_2 was greater than that between CO_2 and Pd at an isosurface of 0.002. This indicates that the electron transfer between Pd and TiO_2 plays a crucial role in the adsorption and activation of CO_2, which had also been detected by XPS characterization. In addition, the charge of a model with both O_{v1} and O_{v2} presented transfers from TiO_2 to Pd, fitting with XPS experimental results indicating that TiO_2 has abundant oxygen vacancies after H_2 treatment.

As shown in Figs. 5(a–c) (considering O_{v12} with both O_{v1} and O_{v2} as an example), electrons were transferred from perfect TiO_2 to CO_2 (0.120 e). When O_v was present, the amount of CO_2 transferred charge also increased to −0.178 e. After Pd loading and hydrogenation treatment, the amount of CO_2 transferred charge reached −0.405 e. Pd was shown to play a very important

Table 1 Adsorption geometry and energy of CO_2 adsorbed on TiO_2 or Pd/H-TiO_2 surface

Model	$d(O_{CO_2}\text{-}Ti_{TiO_2})$/Å	$d(C_{CO_2}\text{-}O_{CO_2})$/Å	$d(C_{CO_2}\text{-}O_{TiO_2})$/Å	∠CO_2(O-C-O)/(°)	$d(Pd\text{-}C_{CO_2})$/Å	E_{ads}/eV
CO_2-TiO_2	2.21/2.21	1.26/1.26	1.42	135.8	–	–0.104
CO_2-H-TiO_2- O_{v1}	2.23/2.20	1.25/1.26	1.41	134.8	–	–0.357
CO_2-H-TiO_2- O_{v2}	2.20/2.30	1.26/1.24	1.45	136.9	–	− 0.312
CO_2-H-TiO_2-$O_{v12}$$^{a)}$	2.21/2.20	1.25/1.26	1.44	136.7	–	− 0.379
CO_2-Pd/TiO_2	–	1.23/1.22	–	145.4	2.05	− 0.412
CO_2-Pd/H-TiO_2-O_{v1}	–	1.28/1.22	–	134.3	2.04	− 0.885
CO_2-Pd/H-TiO_2-O_{v2}	–	1.23/1.23	–	145.4	2.01	− 0.600
CO_2-Pd/H-TiO_2-O_{v12}	–	1.24/1.23	–	143.2	2.01	− 0.114

a) O_{V12} represents a model containing both O_{v1} and O_{v2}.

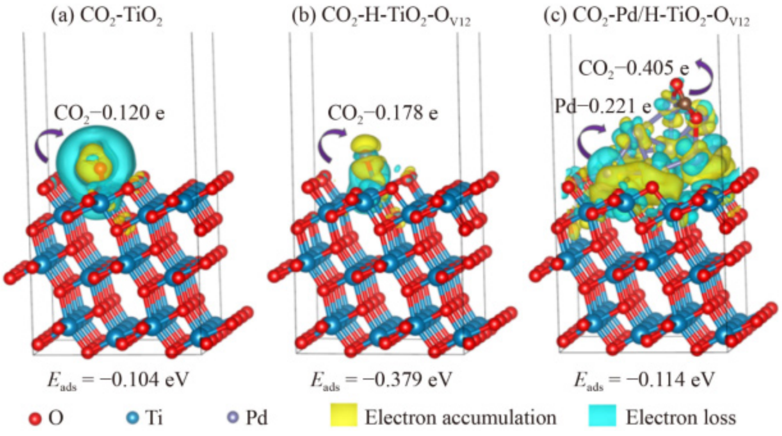

Fig. 5 (a–c) Adsorption configurations of CO_2 with and without O_v and Pd and the charge density difference upon CO_2 adsorption. Yellow and cyan represent electron accumulation and loss, respectively, isosurfaces = 0.0002 e·$Bohr^{-3}$.

role in this process, consistent with the above-mentioned analysis. This also indicated that O_v and Pd were crucial for CO_2 adsorption and activation, leading to excellent HCOOH yields.

3.2.3 Mechanism of the enhanced CO_2 reduction of Pd/H-TiO_2

Generally, it is considered that charge transfer efficiency is an essential influence on the photocatalytic reduction of CO_2 [12]. Photocurrent densities were measured to evaluate photoelectronic properties according to the photocurrent response and PL. The photocurrent response intensity directly reflects photogenerated charge separation efficiency [39]. Figure 6(a) shows the transient photocurrent responses of TiO_2, H-TiO_2, and Pd/H-TiO_2 under UV light irradiation. H-TiO_2 has a higher photocurrent density than TiO_2, indicating that O_v performs the function of separating electron holes. In addition, the Pd/H-TiO_2 catalyst possesses the highest photocurrent density, indicating the higher separation and transfer efficiency of electron-hole pairs leading to superior HCOOH production rates. It has been reported that the rate of charge recombination (~10^{-9} s) is much faster than that of the surface redox process (10^{-8} to 10^{-1} s) [33], such that only electrons migrating to the catalyst surface can participate in the subsequent conversion reactions to product HCOOH. As the number of electrons on the catalyst surface increases, the CO_2 conversion rate increases, which in turn gives higher HCOOH yields. Therefore, excellent electron-hole separation ability is an important prerequisite for high photocatalytic reduction of CO_2 activity. The high photocurrent response of Pd/H-TiO_2 can be ascribed to the role of Pd as the bridge to accelerate photogenerated electron-hole transfers. The electron-hole complexation efficiency was further investigated using PL spectroscopy. Typically, the weaker PL peak represents the lower efficiency of electron-hole complexation under illumination [40,41]. As shown in Fig. 6(b), the increasing order of PL intensities under UV light is Pd/H-TiO_2 < H-TiO_2 < TiO_2, which indicates the presence of O_v and Pd inhibiting the direct compounding of photogenerated electron holes, consistent with transient photocurrent responses. Subsequently, the electrons transferred to the Pd can be used for CO_2 reduction [21,22].

As stated in previous reports, the role of Pd in photocatalytic reaction primarily includes: (i) the separation of electron holes; (ii) enhancing light absorption, thereby generating heat energy due to the localized surface plasmonic resonance (LSPR) effect [42,43]. The role of Pd as an electron trap for electron-hole separation has been demonstrated by PL and photoelectrochemical examinations. To investigate the LSPR effect in Pd/H-TiO_2 under UV light, infrared thermal imaging was used to collect infrared images of sample surfaces in the noncontact mode. As shown in Fig. S8 (cf. ESM), following 30 min of irradiation, the center temperature of the Pd/H-TiO_2 suspension was 26.5 °C, demonstrating that Pd played the role of separating electron-hole under UV light.

3.3 Mechanism of photocatalytic reduction of CO_2 in aqueous systems

We performed diffuse-reflectance infrared Fourier transform spectroscopy (DRIFTS) to further analyze the processes of CO_2 adsorption and activation. Intermediate products of CO_2 conversion in the presence of the Pd/H-TiO_2 catalyst were detected at different times, as shown in Fig. 7. The peaks centered at 1035 and 934 cm^{-1} were ascribed to the adsorbed *HCO_3 and *CO_3, respectively; implying that some CO_2 was converted to HCO_3^- or CO_3^{2-} [44,45]. The characteristic absorption peaks located at 2200–2400 cm^{-1} were ascribed to CO_2 adsorbed onto the Pd/H-TiO_2 catalyst, implying strong CO_2 adsorption on the Pd/H-TiO_2 surface. Peaks centered at 1679 and 1392 cm^{-1} were assigned to the $\nu_{C=O}$ stretching vibration of adsorbed HCOOH and the symmetric stretching vibration of COO^- in *COOH [46].

When inorganic bases and water were used as the reaction system, CO_2 was able to lead to the derivation of multiple intermediates, including carbonate and

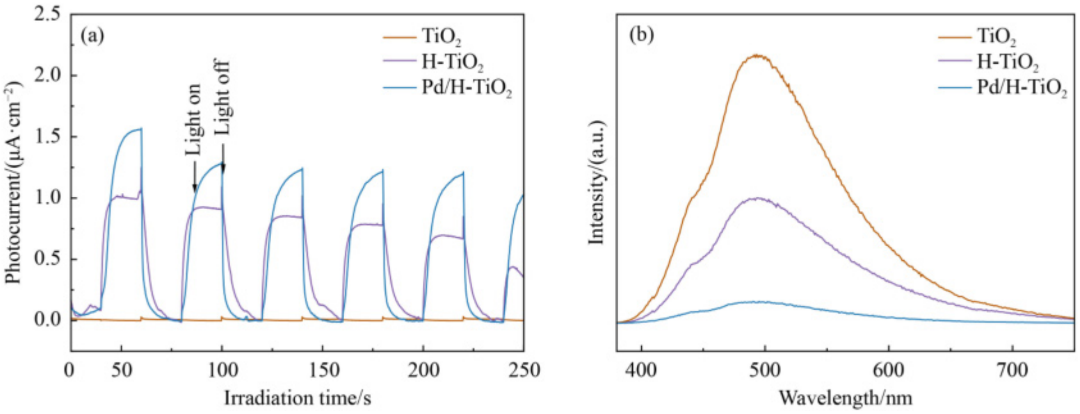

Fig. 6 (a) Transient photocurrent response, (b) PL spectra of TiO_2, H-TiO_2, and Pd/H-TiO_2.

bicarbonate. To verify whether HCO_3^- and CO_3^{2-} participated in the reaction, bicarbonate and carbonate were used in the photocatalytic reaction (Fig. S9, cf. ESM). Our results showed that a small amount of HCOOH was produced. From the above results, it can be concluded that there are three intermediate species in photocatalytic reduction in the presence of a Pd/H-TiO_2 catalyst. The process may include the adsorption of CO_2 onto a TiO_2 surface, which quickly reaches equilibrium, causing some of the CO_2 to be converted to CO_3^{2-} and HCO_3^-, which then participate in the reaction.

Combining the characterization, DFT calculation, and experimental analyses outlined above, a reaction mechanism was proposed as illustrated in Fig. 8. The reaction stage of photocatalytic reduction of CO_2 to HCOOH contained the CO_2 adsorption activation stage on the surface and the reduction reaction stage. First, CO_2 and H_2 molecules were co-adsorbed onto the surface of the catalyst. TiO_2 was excited under UV irradiation to produce electron-hole pairs to participate in the reaction (Eq. (4)). Photogenerated electron-hole pairs were then transferred to the surface of the catalyst in order to activate CO_2 and H_2 molecules to form active species of $^*CO_2$ and H [47]. Subsequently, *COOH intermediates formed by the transfer of H atoms in H_2 to O atoms of CO_2 led to their conversion from intermediates to the target product of HCOOH (Eq. (5)). H_2O molecules were oxidized by h^+ to form OH groups (Eq. (6)).

$$TiO_2 + h\nu \rightarrow e^- + h^+, \tag{6}$$

$$CO_2 + 2e^- + 2H^+ \rightarrow HCOOH_{(aq)}, \tag{7}$$

$$h^+ + H_2O \rightarrow \cdot OH + H^+ \tag{8}$$

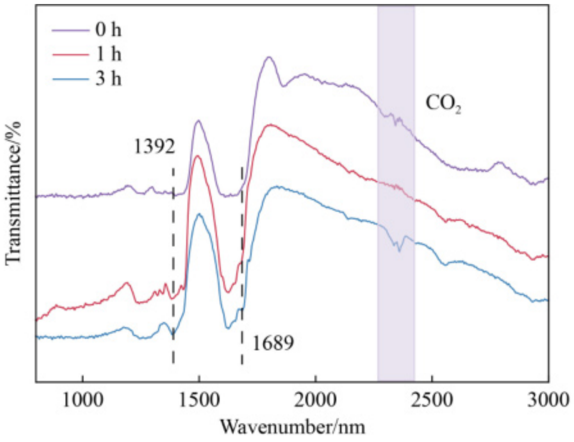

Fig. 7 DRIFTS spectra of the Pd/H-TiO_2 catalyst after the photocatalytic reaction.

4 Conclusions

The Pd/H-TiO_2 catalyst was successfully prepared via a facile impregnation method combined with a hydrogen treatment process. In the presence of an appropriate base, the yield of HCOOH over a Pd/H-TiO_2 catalyst reached 14.14 mmol·g_{cat}^{-1}·h^{-1} and the HCOOH selectivity was close to 100%. Experimental characterizations and theoretical calculations demonstrated that this superior activity was derived from the synergistic effect of Pd and O_v. In particular, O_v could increase CO_2 adsorption, while Pd loading was beneficial for electron-hole pair separation. The transfer of electrons from the support to Pd played a crucial role in promoting CO_2 activation.

Competing interests The authors declare that they have no competing interests.

Acknowledgements This work was financially supported by the National Key Research and Development Program of China (Grant No. 2022YFE0208400), the Natural Science Foundation of Shanxi Province (Grant No. 202303021221019), the Fundamental Research Funds for the Central Universities (Grant No. 2022ZFJH004), and the Shanxi-Zheda Institute of Advanced Materials and Chemical Engineering (Grant No. 2021SX-FR002).

Electronic Supplementary Material Supplementary material is available in the online version of this article at https://doi.org/10.1007/s11705-024-2485-2 and is accessible for authorized users.

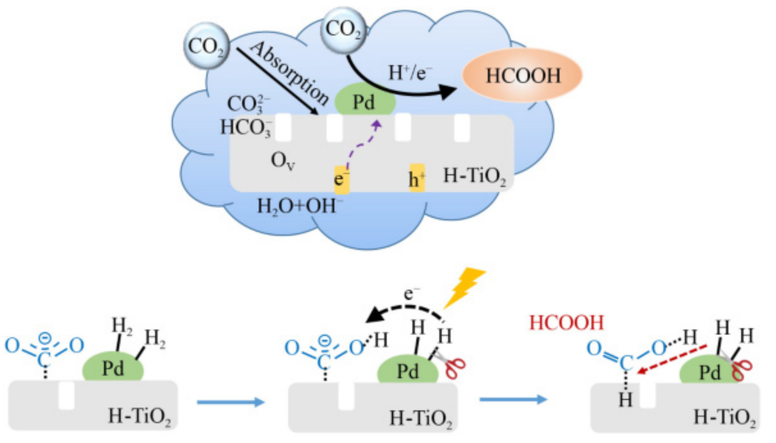

Fig. 8 Mechanism of the photocatalysis of CO_2 to produce HCOOH.

References

1. Yuan Z M, Zhu X L, Gao X Q, An C H, Wang Z, Zuo C, Dionysiou D D, He H, Jiang Z Y. Enhancing photocatalytic CO_2 reduction with TiO_2-based materials: strategies, mechanisms, challenges, and perspectives. Environmental Science and Ecotechnology, 2024, 20: 100368
2. Wang S W, Wang L G, Wang D S, Li Y D. Recent advances of single-atom catalysts in CO_2 conversion. Energy & Environmental Science, 2023, 16(7): 2759–2803
3. Pan F P, Li B Y, Deng W, Du Z C, Gang Y, Wang G F, Li Y. Promoting electrocatalytic CO_2 reduction on nitrogen-doped carbon with sulfur addition. Applied Catalysis B: Environmental, 2019, 252: 240–249
4. Liu M X, Xu Y K, Meng Y, Wang L J, Wang H, Huang Y C, Onishi N, Wang L, Fan Z J, Himeda Y. Heterogeneous catalysis for carbon dioxide mediated hydrogen storage technology based on formic acid. Advanced Energy Materials, 2022, 12(31): 2200817
5. Lv C C, Bai X H, Ning S B, Song C X, Guan Q Q, Liu B, Li Y G, Ye J H. Nanostructured materials for photothermal carbon dioxide hydrogenation: regulating solar utilization and catalytic performance. ACS Nano, 2023, 17(3): 1725–1738
6. Zhang S Q, Yu H Y, Wang Y, Yan Y X, Dai J, Shu D J, Wu X L. Surface dual metal occupations in Fe-doped $Fe_xBi_{2-x}O_3$ induce highly efficient photocatalytic CO_2 reduction. ACS Applied Materials & Interfaces, 2023, 15(20): 25049–25057
7. Saito D, Tamaki Y, Ishitani O. Photocatalysis of CO_2 reduction by a Ru(II)-Ru(II) supramolecular catalyst adsorbed on Al_2O_3. ACS Catalysis, 2023, 13(7): 4376–4383
8. Pan H Q, Heagy M D. Photons to formate: a review on photocatalytic reduction of CO_2 to formic acid. Nanomaterials, 2020, 10(12): 2422
9. Xiong J, Yang A J, Sun Q, Gao H X, Zhang H Y, Mao Y, Liang Z W. Insights into CO_2 activation and charge transfer in photocatalytic reduction of CO_2 on pure and metal single atom modified TiO_2 surfaces. Molecular Catalysis, 2023, 547: 113370
10. Khan H, Shah M U H. Modification strategies of TiO_2 based photocatalysts for enhanced visible light activity and energy storage ability: a review. Journal of Environmental Chemical Engineering, 2023, 11(6): 111532
11. Li G H, Sun Y Y, Zhang Q M, Gao Z, Sun W, Zhou X X. Ag quantum dots modified hierarchically porous and defective TiO_2 nanoparticles for improved photocatalytic CO_2 reduction. Chemical Engineering Journal, 2021, 410: 128397
12. Wu Y W, Yan L, Yu Y Q, Jing C Y. Photocatalytic CO_2 reduction to CH_4 on iron porphyrin supported on atomically thin defective titanium dioxide. Catalysis Science & Technology, 2021, 11(18): 6103–6111
13. Ali Khan A, Tahir M. Synergistic effect of Co/La in oxygen vacancy rich ternary CoAlLa layered double hydroxide with enhanced reductive sites for selective photoreduction of CO_2 to CH_4. Energy & Fuels, 2021, 35(10): 8922–8943
14. Zhao H L, Pan F P, Li Y. A review on the effects of TiO_2 surface point defects on CO_2 photoreduction with H_2O. Journal of Materiomics, 2017, 3(1): 17–32
15. Song G X, Lang X F, Huo C X, Ren S H, Wang Y J, Tang Z K, Chen X G. Mechanism of photocatalytic reduction of CO_2 to CH_4 on F-doped defective anatase TiO_2 (101) surface: a density functional theory study. Surface Science, 2023, 730: 122247
16. Wang S, Nie X W, Lin J B, Ding F S, Song C S, Guo X W. Computational design of single-atom modified Ti-MOFs for photocatalytic CO_2 reduction to C1 chemicals. ChemSusChem, 2024, 17(8): e202301619
17. Wei F, Luo T, Wang Y, Kong L C, Feng J J, Li Z Q, Lu J Q, Yang F. Boosting CO_2 electroreduction to formate via *in-situ* formation of ultrathin Bi nanosheets decorated with monodispersed Pd nanoparticles. Journal of Catalysis, 2023, 424: 50–63
18. Zhang F, Li Y H, Qi M Y, Tang Z R, Xu Y J. Boosting the activity and stability of Ag-Cu_2O/ZnO nanorods for photocatalytic CO_2 reduction. Applied Catalysis B: Environmental, 2020, 268: 118380
19. Shi Y X, Li L L, Xu Z, Guo F, Li Y, Shi W L. Synergistic coupling of piezoelectric and plasmonic effects regulates the Schottky barrier in Ag nanoparticles/ultrathin g-C_3N_4 nanosheets heterostructure to enhance the photocatalytic activity. Applied Surface Science, 2023, 616: 156466
20. Jin B B, Ye X, Zhong H, Jin F M. Light-driven hydrogenation of bicarbonate into formate over nano-Pd/TiO_2. ACS Sustainable Chemistry & Engineering, 2020, 8(17): 6798–6805
21. Zheng M Y, Yang J, Fan W L, Zhao X. Oxygen vacancy and nitrogen doping collaboratively boost performance and stability of TiO_2-supported Pd catalysts for CO_2 photoreduction: a DFT study. Physical Chemistry Chemical Physics, 2021, 23(43): 24801–24813
22. Li J, Zhou H, Zhuo H, Wei Z Z, Zhuang G L, Zhong X, Deng S W, Li X N, Wang J G. Oxygen vacancies on TiO_2 promoted the activity and stability of supported Pd nanoparticles for the oxygen reduction reaction. Journal of Materials Chemistry. A, Materials for Energy and Sustainability, 2018, 6(5): 2264–2272
23. Vequizo J J M, Kato K, Amano F, Yamakata A. Unfolding the impact of H_2-reduction treatment in enhancing the photocatalytic activity of rutile TiO_2 based on photocarriers dynamics. Journal of Physical Chemistry C, 2023, 127(22): 10411–10418
24. Sang L X, Zhao Y X, Burda C. TiO_2 nanoparticles as functional building blocks. Chemical Reviews, 2014, 114(19): 9283–9318
25. Zhong J B, Lu Y, Jiang W D, Meng Q M, He X Y, Li J Z, Chen Y Q. Characterization and photocatalytic property of Pd/TiO_2 with the oxidation of gaseous benzene. Journal of Hazardous Materials, 2009, 168(2-3): 1632–1635
26. Yilmaz P, Lacerda A M, Larrosa I, Dunn S. Photoelectrocatalysis of rhodamine B and solar hydrogen production by TiO_2 and Pd/TiO_2 catalyst systems. Electrochimica Acta, 2017, 231: 641–649
27. Phan T N, Park Y K, Lee I G, Ko C H. Enhancement of C–O bond cleavage to afford aromatics in the hydrodeoxygenation of anisole over ruthenium-supporting mesoporous metal oxides. Applied Catalysis A, General, 2017, 544: 84–93
28. Samsudin E M, Hamid S B A, Juan J C, Basirun W J, Kandjani A E. Surface modification of mixed-phase hydrogenated TiO_2 and

corresponding photocatalytic response. Applied Surface Science, 2015, 359: 883–896

29. Liu L, Yu P Y, Chen X B, Mao S S, Shen D Z. Hydrogenation and disorder in engineered black TiO_2. Physical Review Letters, 2013, 111(6): 065505
30. Mo L B, Wang Y, Bai Y, Xiang Q Y, Li Q, Yao W Q, Wang J O, Ibrahim K, Wang H H, Wan C H, et al. Hydrogen impurity defects in rutile TiO_2. Scientific Reports, 2015, 5(1): 17634
31. Zhang Y S, Liu J X, Qian K, Jia A P, Li D, Shi L, Hu J, Zhu J F, Huang W X. Structure sensitivity of Au-TiO_2 strong metal-support interactions. Angewandte Chemie International Edition, 2021, 60(21): 12074–12081
32. Li J L, Zhang M, Guan Z J, Li Q Y, He C Q, Yang J J. Synergistic effect of surface and bulk single-electron-trapped oxygen vacancy of TiO_2 in the photocatalytic reduction of CO_2. Applied Catalysis B: Environmental, 2017, 206: 300–307
33. Jiang D L, Zhou Y M, Zhang Q X, Song Q, Zhou C J, Shi X L, Li D. Synergistic integration of AuCu Co-catalyst with oxygen vacancies on TiO_2 for efficient photocatalytic conversion of CO_2 to CH_4. ACS Applied Materials & Interfaces, 2021, 13(39): 46772–46782
34. Zhu Q H, Deng Z S, Xie H J, Xing M Y, Zhang J L. Investigation of concerted proton-electron donors for promoting the selective production of HCOOH in CO_2 photoreduction. ACS Catalysis, 2023, 13(5): 3254–3262
35. Peña R, Romero R, Amado-Piña D, Natividad R. Cu/TiO_2 photo-catalyzed CO_2 chemical reduction in a multiphase capillary reactor. Topics in Catalysis, 2024, 67(5-8): 377–393
36. Zhang H N, Li Y F, Wang J Z, Wu N N, Sheng H, Chen C C, Zhao J C. An unprecedent hydride transfer pathway for selective photocatalytic reduction of CO_2 to formic acid on TiO_2. Applied Catalysis B: Environmental, 2021, 284: 119692
37. Iguchi S, Kikkawa S, Teramura K, Hosokawa S, Tanaka T. Investigation of the electrochemical and photoelectrochemical properties of Ni-Al LDH photocatalysts. Physical Chemistry Chemical Physics, 2016, 18(20): 13811–13819
38. Huang X Y, Lei R, Yuan J, Gao F, Jiang C K, Feng W H, Zhuang J D, Liu P. Insight into the piezo-photo coupling effect of $PbTiO_3$/CdS composites for piezo-photocatalytic hydrogen production. Applied Catalysis B: Environmental, 2021, 282: 119586
39. Zheng D, Xue Y F, Wang J, Varbanov P S, Klemes J J, Yin C. Nanocatalysts in photocatalytic water splitting for green hydrogen generation: challenges and opportunities. Journal of Cleaner Production, 2023, 414: 137700
40. Quan Q, Xie S J, Weng B, Wang Y, Xu Y J. Revealing the double-edged sword role of graphene on boosted charge transfer versus active site control in TiO_2 nanotube arrays@RGO/MoS_2 heterostructure. Small, 2018, 14(21): 1704531
41. Basumatary R, Basumatary B, Konwar D, Ramchiary A. Tailored highly efficient Co-doped TiO_2/$CoTiO_3$ heterojunction photocatalyst for methylene blue degradation under visible light. Journal of the Korean Ceramic Society, 2023, 60(3): 547–559
42. Ren J, Ouyang S, Xu H, Meng X, Wang T, Wang D, Ye J. Targeting activation of CO_2 and H_2 over Ru-loaded ultrathin layered double hydroxides to achieve efficient photothermal CO_2 methanation in flow-type system. Advanced Energy Materials, 2017, 7(5): 1601657
43. Chang L, Besteiro L V, Sun J C, Santiago E Y, Gray S K, Wang Z M, Govorov A O. Electronic structure of the plasmons in metal nanocrystals: fundamental limitations for the energy efficiency of hot electron generation. ACS Energy Letters, 2019, 4(10): 2552–2568
44. Cao Y H, Zhang R Y, Zhou T L, Jin S M, Huang J D, Ye L Q, Huang Z A, Wang F, Zhou Y. Zhou Y. B–O bonds in ultrathin boron nitride nanosheets to promote photocatalytic carbon dioxide conversion. ACS Applied Materials & Interfaces, 2020, 12(8): 9935–9943
45. Zindrou A, Deligiannakis Y. Quantitative *in situ* monitoring of Cu-atom release by Cu_2O nanocatalysts under photocatalytic CO_2 reduction conditions: new insights into the photocorrosion mechanism. Nanomaterials (Basel, Switzerland), 2023, 13(11): 1773
46. Li A, Cao Q, Zhou G Y, Schmidt B, Zhu W J, Yuan X T, Huo H L, Gong J L, Antonietti M. Three-phase photocatalysis for the enhanced selectivity and activity of CO_2 reduction on a hydrophobic surface. Angewandte Chemie International Edition, 2019, 58(41): 14549–14555
47. Qu T X, Wei S Z, Xiong Z, Zhang J Y, Zhao Y C. Progress and prospect of CO_2 photocatalytic reduction to methanol. Fuel Processing Technology, 2023, 251: 107933